



HAL
open science

Revealing soot maturity based on multi-wavelength absorption/emission measurements in laminar axisymmetric coflow ethylene diffusion flames

Jérôme Yon, Juan José Cruz, Felipe Escudero, José Morán, Fengshan Liu, Andrés Fuentes

► To cite this version:

Jérôme Yon, Juan José Cruz, Felipe Escudero, José Morán, Fengshan Liu, et al.. Revealing soot maturity based on multi-wavelength absorption/emission measurements in laminar axisymmetric coflow ethylene diffusion flames. *Combustion and Flame*, 2021, 227, pp.147-161. 10.1016/j.combustflame.2020.12.049 . hal-03112768

HAL Id: hal-03112768

<https://normandie-univ.hal.science/hal-03112768>

Submitted on 3 Feb 2023

HAL is a multi-disciplinary open access archive for the deposit and dissemination of scientific research documents, whether they are published or not. The documents may come from teaching and research institutions in France or abroad, or from public or private research centers.

L'archive ouverte pluridisciplinaire **HAL**, est destinée au dépôt et à la diffusion de documents scientifiques de niveau recherche, publiés ou non, émanant des établissements d'enseignement et de recherche français ou étrangers, des laboratoires publics ou privés.



Distributed under a Creative Commons Attribution - NonCommercial 4.0 International License

Revealing Soot Maturity Based on Multi-Wavelength Absorption/Emission Measurements in Laminar Axisymmetric Coflow Ethylene Diffusion Flames

Jérôme Yon^{a,*}, Juan José Cruz^b, Felipe Escudero^b, José Morán^a, Fengshan Liu^c, Andrés Fuentes^{b,*}

^a*Normandie Univ, UNIROUEN, INSA Rouen, CNRS, CORIA, 76000 Rouen, France.*

^b*Departamento de Industrias, Universidad Técnica Federico Santa María, Av. España 1680, Casilla 110-V, Valparaíso, Chile.*

^c*Metrology Research Centre, National Research Council of Canada, Ottawa, Ontario, Canada.*

Abstract

A novel diagnostic is proposed to characterize the maturity of soot particles in a laminar axisymmetric coflow ethylene diffusion flame in terms of the spectral dependence of soot absorption function. The method relies on the combination of line-of-sight attenuation (LOSA) and emission measurements at four wavelengths (500, 532, 660 and 810 nm). The analysis of the measured signals enables the determination of soot temperature, soot volume fraction, soot maturity and the contribution of soot scattering to extinction. The analysis of extinction and emission measurements considers the spatial variation of soot optical properties. The introduction of a maturity index allows the evaluation of soot maturity based on the spectral variation of the soot absorption function. The maturity index is correlated with the organic or the mature soot content and finally in terms of the absolute value of absorption function at 810 nm. The methodology is validated using a set of synthetic spectral LOSA and emission signals representing experimental measurements based on numerical results obtained using the CoFlame code. A sensitivity analysis of the Abel inversion is also performed to properly address the effect of deconvolution procedure. Finally, the proposed method is applied to analyze the experimental data of spectrally-resolved LOSA and emission acquired in a laminar axisymmetric coflow ethylene diffusion flame

*Corresponding authors. *E-mail addresses:* yon@coria.fr and andres.fuentes@usm.cl

established on a Gülder burner. The two-dimensional distributions of soot temperature, soot volume fraction, soot maturity, and the ratio of total scattering to absorption are determined. Mature soot particles are found on the top of the flame in the centerline region and also in the outer edge of the flame wing displaying strong gradients.

Keywords: soot maturity, LOSA, pyrometry, absorption function

1. Introduction

Ultrafine soot particles released from combustion systems as a result of incomplete oxidation have a negative impact on both human health [1] and climate change [2]. These concerns of the effects of soot released to the environment have brought the implementation of increasingly more stringent emission regulations [3], whereas the toxicological issues and mechanisms involved in global warming of combustion-generated soot are not yet elucidated due to the complex composition and morphology of soot aggregates [4]. Also, due to its significant contribution to radiative heat transfer in combustion systems, it is desirable to produce soot to enhance heat transfer [5]. Therefore, it is important to develop capabilities to control the production of soot in certain applications while reducing soot emissions to the environment. To this end, it is critical to develop optically-based diagnostics to measure various soot properties. The detailed soot characterization in flames helps not only to understand soot formation mechanisms but also to validate soot models in terms of prediction of soot volume fraction, morphology, and maturity in CFD applications.

The process of soot formation can be pictured as a sequence of steps beginning with the birth of incipient soot particles, also known as nascent soot [6]. The incipient particles undergo subsequent surface chemical reactions as well as surface condensation of polycyclic aromatic hydrocarbons (PAHs), transforming incipient soot particles into young soot [7, 8]. The second step is the further growth of particles due to surface reactions and clusters aggregation. The last step takes place at high temperatures and in the presence of oxidative compounds (mainly O_2 , OH , among others, especially on the oxidizer side of the reaction zone). The soot oxidation process consumes all or a portion of the soot generated in the previous steps and affects their size by mass consumption and particle fragmentation. These three steps (inception, growth and oxidation) are schematically illustrated with a

sequential dependence on the height above the burner (HAB) as shown in the center of Fig. 1. Clearly, the actual phenomena of these competing and simultaneously-occurring processes are more complex than the simplified representation given in this figure.

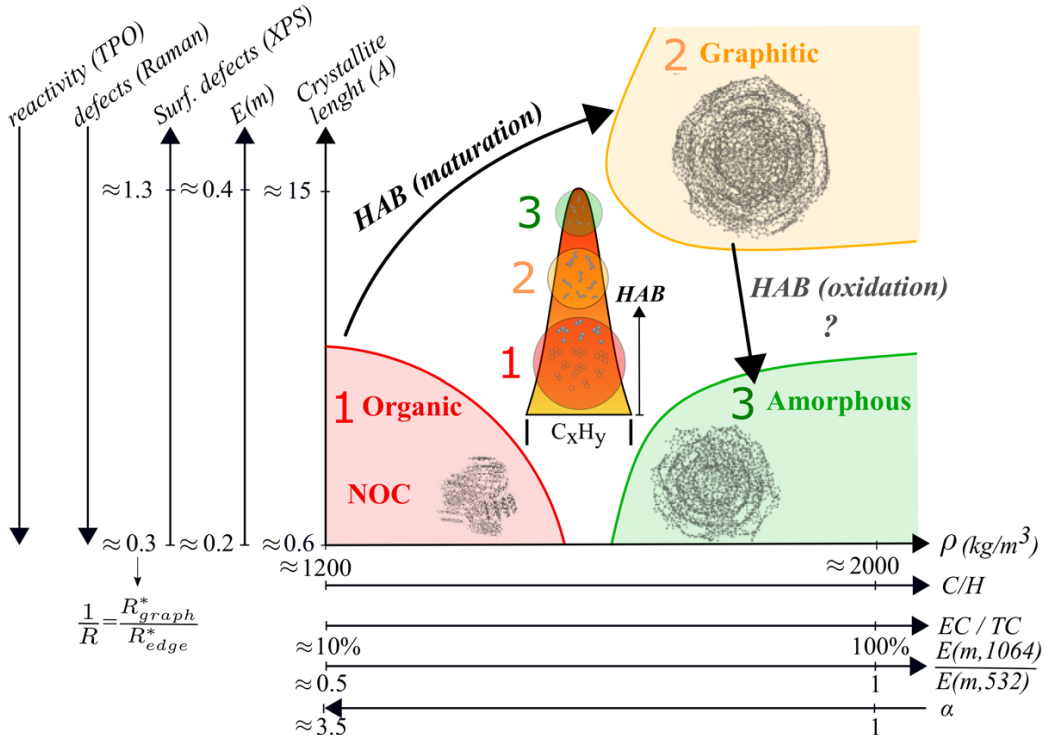


Figure 1: Evolution of soot properties with HAB and soot maturity. Illustrations of microstructures in the three zones (1: inception, 2: surface growth, and 3: oxidation) are adapted from [9, 10].

According to Michelsen et al. [11], "maturity level of a soot particle describes how much it has evolved from inception toward a fully mature graphite-like particle". The evolution of soot maturity is accompanied by changes in various physical and chemical properties of soot particles, such as carbon-atom structure, carbon-to-hydrogen (C/H) ratio, and refractive index. Different experimental methods have been used to probe soot maturity. Baldelli et al. [12] recently reviewed different *ex-situ* techniques that can be employed to characterize the soot maturity. Most of the related measurands and their variation trends during soot lifetime are illustrated in Fig. 1.

We will first discuss soot quantities listed on the abscissa of Fig. 1. The

organic carbon (OC) contents of soot particles at the early stage of formation, which include saturated and unsaturated hydrocarbons, aliphatics, aromatics, PAHs, and oxidized organics that have condensed onto soot particles, are fairly volatile [13]. On the contrary, the elemental or refractory carbon (EC) is stable in the high-temperature flame environment. In this context, a thermal/optical reflectance (TOR) analysis allows the mass of OC or EC compared to the total soot particle carbon mass (TC) to be quantified [14, 15]. As a result of carbonization, the EC content or the EC/TC ratio in Fig. 1, increases with increasing level of soot maturity as measured by light extinction [16]. Also, C/H increases as a result of soot dehydrogenation process [17], losing H atoms while raising the amount of carbon SP^2 [18]. As a consequence of the change of composition, the soot particle bulk density (ρ) also evolves. The bulk density of organic materials is lower than that of graphite-like microcrystalline structures but similar to that of PAHs (around 1200 kg/m^3); meanwhile the bulk density of pure graphite or amorphous carbon aggregates can reach 2000 kg/m^3 (see respectively [19] and [20]). A recent study has shown the important role played by the OC/TC ratio to soot particle bulk density [21].

Naturally, the change of composition also affects the ability of the particle to absorb light. The mass absorption cross section (absorption cross section per unit mass of particles, MAC) is related to the particle absorption efficiency. Additionally, MAC can be related to the $E(m)/\rho$ ratio, with $E(m)$ being the soot absorption function. The MAC of black carbon (terminology similar to mature soot in the aerosol, atmospheric science, and environmental science communities) has been recently reviewed by Liu et al. [22], who recommended a value of $8.0 \pm 0.7 \text{ m}^2/\text{g}$ at 550 nm wavelength. In this review, the authors also revised the most probable absorption function to $E(m) \approx 0.4$ at the wavelength of 532 nm and recommended wavelength independent $E(m)$ in the visible and near infrared (NIR) spectrum. It is important to point out that the presence of organics leads to a decrease in $E(m)$, especially at longer wavelengths in the NIR spectrum. Therefore, organic materials, including nano-organic carbon (NOC) [23], are characterized by a strong spectral dependence of $E(m)$ compared to mature soot (quantified by the Angström or dispersion exponent α) as consistently shown by different studies [13, 24–29]. This spectral dependence of the absorption efficiency can be represented by $E(m, 1064)/E(m, 532)$ and α in the abscissa of Fig. 1.

The strong spectral dependence of organic materials is responsible of their

common brown-carbon aspect. The spectral dependence of $E(m)$ can be determined by the two excitation wavelengths LII (TEW-LII) technique introduced by Therssen et al. [30], enabling to establish the ratio of $E(m)$ at the two laser wavelengths. This method can be used to determine the spectral dependence of soot absorption as shown for both premixed [31] and diffusion flames [32]. In contrast to their weak absorption efficiency, organic materials have a high scattering efficiency and could be detected by simple extinction measurements, whereas the LII technique fails. This principle is used by Leschowski et al. [33] to reveal the soot maturation process. Based on extinction-calibrated LII and cavity ring-down extinction (CRDE) optical techniques, Betrancourt et al. [34] estimated the level of soot maturity quantitatively together with the soot volume fraction profiles in two *n*-butane premixed flames.

We now discuss the effects of soot internal microstructure on soot properties listed on the ordinate axis of Fig. 1 during the evolution of soot in flames. Graphitic soot particles generally display an onion-shaped arrangement of carbon atoms with large and parallel crystallites on the surface of primary particles [35]. This feature can be observed by high resolution transmission electron microscopy (HRTEM) images as done in both premixed [6], and diffusion flames [36]. In consequence, many studies characterize soot maturity in terms of the level of particle graphitization [37] that can be also revealed by Raman scattering, since its signature reveals the degree of order of the material and can be correlated to the crystallite lengths [38]. In this sense, less mature soot particles are composed of amorphous carbon which displays no particular order [18]. The change of internal carbon atom order appears to be correlated to the change of carbon reactivity as revealed by temperature programmed oxidation (TPO) studies [39]. It should be pointed out that for a given amount of organics the impact of the degree of graphitization, i.e., the transition from an amorphous to a graphitized structure, on the optical properties is not well established. Numerical simulations tended to show an impact, in particular in the UV spectral region [10]. Available experiments revealed that amorphous carbon particles generated by spark discharges of monolithic graphite are less light-absorbing, i.e., they display a lower $E(m)$ than graphitic soot particles as commonly generated in ethylene diffusion flames [40]. This has also been observed in certain premixed methane flames [41]. In this case, however, it cannot be excluded that soot particles also experience a change in the organic content. Nevertheless, contrary to the presence of organic compounds, the degree of graphitiza-

tion (from amorphous to graphitic carbon [11]) does not seem to affect the spectral dependence of $E(m)$ [40].

The grouping of measurands listed in the x or y axes in Fig. 1 is motivated by the specific role played by oxidation. Indeed, it is noticed that graphitic soot composed of large crystallites can evolve towards shorter and less ordered ones, which are more strongly affected by oxidizing environments [42]. OH radicals or O₂ molecules can pull-up some carbon atoms resulting in their deformation and a decrease of the size of crystallites. This process causes the appearance of defects in the crystalline structure, which can be clearly observed by Raman scattering measurements [39]. These defects on the particle surface have also been highlighted by X-ray photoelectron spectroscopy (XPS) as proposed by Ouf et al. [43]. Therefore, it is suspected that the oxidation process, which tends to transform graphitic soot to amorphous soot, causes a decrease of $E(m)$ but weakly affects its spectral dependence. Consequently, it is important to point out that certain soot measurands, such as EC/TC ratio and the spectral dependence of $E(m)$ as measured by TEW-LII, are unable to characterize the microstructure of carbon atoms (graphitic or amorphous) or the degree of soot oxidation.

In the last two decades, significant progress has been achieved on the characterization of physico-chemical properties of soot particles and how they evolve in flames. The understanding has been gained mainly by investigating laminar diffusion flames for maturity. Studies have been performed by extinction measurements in a triple co-flow burner [44], extinction and Raman spectroscopy on laser-irradiated soot sampled in ethylene and methane diffusion flames [28]. Transmission Electron Microscopy (TEM) has been widely used in co-flow diffusion flames [45], kerosene and n-decane flames [36], inverted gravity flame reactor [46], in the centerline of ethylene, propane and butane diffusion flames [47] and also by varying the pressure in the combustion chamber [48]. Nascent soot formation has been investigated by TEM in buoyancy dominated ethene, methane and acetylene diffusion flames [7], by fluorescence, laser light extinction and scattering in a methane/oxygen flame [8]. Soot reactivity has been investigated by varying the oxygen content or the fuel composition and coupling different physico-chemical analysis techniques [49].

Optical diagnostics of soot in flames are important because of their quasi non-intrusive nature that allows to acquire information in flames without perturbing it [50]. Nevertheless, studies devoted to characterization of soot maturity in flames using optical methods are relatively scarce and generally

suffer from low to no spatial resolution.

The objective of the present work is to develop and demonstrate a non-intrusive experimental technique with high spatial resolution for the *in-situ* evaluation of soot maturity in axisymmetric laminar flames. This objective is achieved by coupling line-of-sight attenuation (LOSA) and flame emission measurements at multi-wavelengths (two or more) in the visible and near IR spectrum. Specifically, the present work was conducted at four wavelengths. Using the proposed method, we can obtain different soot properties (temperature, volume fraction, and ratios of $E(m)$ at different pairs of detection wavelengths) with a high spatial resolution as compared to TEW-LII or other available methods. Moreover, this method is less intrusive than LII-based techniques that may modify the soot particle structure and optical properties as a result of intense laser heating. Indeed, soot particle graphitization has been found to increase with increasing laser fluence [51]. Additionally, a novel approach is developed to obtain the spectrally-resolved absolute $E(m)$ values. This is achieved by assuming that the soot maturation process is limited to the path 1 \rightarrow 2 as presented in Fig. 1, i.e., without considering the oxidation-induced evolution from graphitic to amorphous structure. It is possible to estimate $E(m)$ by proposing a functional relationship that is able to convert a quantity in the x axis to a quantity in the y axis in Fig. 1, without requiring any additional measurements. The functional relationship for the conversion is based on the study of Bescond et al. [40], who carefully determined the absolute variation of soot refractive index and its spectral dependence in the visible range for three surrogates representative of organic, graphitic, and amorphous soot by hypothesising that the spark-discharged carbon nanoparticles can be considered as a surrogate of amorphous soot. Moreover, it was also shown by Bescond et al. [40] that the mixing laws enabled the determination of the refractive index of any soot type of known composition as a function of the volume fraction of each surrogate. This finding will be used in the present work to evaluate a spatially-resolved distribution of $E(m)$ based on combined LOSA and emission measurements at the four wavelengths under the limitation that the present study considers only the organic and graphitic components. Finally, it will be shown for the first time that neglecting the spatial variation of $E(m)$ in a laminar coflow diffusion flame has a significant influence on the measurements of soot temperature and volume fraction using optical diagnostics, such as two-color soot pyrometry, LII, and extinction methods.

2. Methodology

After Abel inversion of the experimental LOSA images (expressed in terms of light transmissivity τ_λ) and the line-of-sight integrated flame emission (P_λ) at each of the four detection wavelengths, the local extinction coefficient (k_{ext}) and emission rate can be obtained [52],

$$\begin{aligned} k_{ext}(r, z, \lambda) &= k_{abs}(r, z) \times (1 + \alpha_\lambda) \\ k_{abs}(\lambda) &= \frac{6\pi E(m) f_v}{\lambda} \\ J(r, z, \lambda) &= \gamma k_{abs}(r, z) \times B(T(r, z), \lambda), \end{aligned} \quad (1)$$

where k_{abs} is the absorption coefficient, r is the radial distance from the flame axis and z is the Height Above the Burner (also referred as HAB), α_λ is the ratio of the total scattering coefficient to the absorption coefficient at a given wavelength λ , $E(m)$ is the soot absorption function dependent on soot refractive index m , f_v is the soot volume fraction, γ is a calibration factor, J is the Abel inverted local thermal emission rate, B is the Planck's blackbody spectral intensity, and T is the local soot temperature. Details of the inversion procedure are given in Section 3 and Appendix C. It is noticed that the scattering contribution to extinction is increasingly important with decreasing wavelength and is not negligible at relatively short wavelengths below about 800 nm.

2.1. Soot temperature

Soot is assumed to be in thermal equilibrium with gas in flames and its temperature can be commonly determined by two-color (2C) pyrometry based on the ratio of emission rates at two detection wavelengths [53]:

$$T_{2C, \lambda_1 - \lambda_2} \approx \left(\frac{k_b}{hc (\lambda_1^{-1} - \lambda_2^{-1})} \ln \left(\frac{J_{\lambda_2}}{J_{\lambda_1}} \left(\frac{\lambda_2}{\lambda_1} \right)^6 \right) \right)^{-1}, \quad (2)$$

where k_b and h are the Boltzmann and Planck constants, respectively, and c is the speed of light. It is noticed that some important assumptions are commonly employed when using this expression, such as neglecting the wavelength dependence of $E(m)$ and the attenuation of flame emission. The former assumption is commonly believed to be valid for mature soot, in particular at longer wavelengths (upper limit of visible and NIR). The validity

of this assumption is discussed later. The latter assumption is in general valid for atmospheric laminar diffusion flames including the one investigated in this study. An alternative method for determining soot temperature is to combine absorption (extinction measured at a wavelength around 800 nm) and emission measurements at the same wavelength:

$$T_{J/k_{abs}} = \left(-\frac{k_b \lambda}{hc} \ln \left(\frac{\lambda^5 J}{2hc^2 \gamma k_{abs}} \right) \right)^{-1}. \quad (3)$$

This approach enables the determination of soot temperature without the need for assuming the value and wavelength dependence of soot $E(m)$. However, an absolute calibration of emission measurements for determining the calibration parameter γ is required. In the present study, a relative calibration for each pair of detection wavelengths is conducted but the absolute value of γ is not determined. Consequently, it is necessary to introduce a criterion that will be defined below.

The above expression can be used to determine the soot temperature based on coupled emission/extinction measurements when the contribution of total scattering can be considered negligible. This should be the case when measurements are conducted at relatively long wavelengths, namely at 810 nm in this work. Otherwise, the scattering contribution to extinction expressed in terms of α_λ has to be considered.

2.2. Scattering contribution

When the calibration constant γ is determined, Eq. 1 can be used to obtain the ratio of total soot scattering to absorption:

$$\alpha_\lambda = \gamma \frac{k_{ext}}{J} B(T, \lambda) - 1. \quad (4)$$

2.3. Soot absorption function and maturity

We can re-write the ratio of emissions in terms of ratio of $E(m)$:

$$\frac{E(m, \lambda_1)}{E(m, \lambda_2)} = \frac{J(\lambda_1) \lambda_1 B(T, \lambda_2)}{J(\lambda_2) \lambda_2 B(T, \lambda_1)}. \quad (5)$$

It is well known that a pronounced spectral dependence of the absorption function is a distinct feature of organic materials (as discussed in Section 1). On one hand, the $E(m)$ ratio at two different wavelengths can be quantified

by determining the Angström absorption exponent, which characterizes the deviation of soot absorption function from an inversely proportional dependence on wavelength, as expected for mature soot ($E(m)$ constant) in the Rayleigh scattering regime. On the other hand, in this study we prefer to characterize the degree of soot maturity by quantifying the spectral dependence of $E(m)$. Specifically, we introduce a parameter β defined below for this purpose:

$$\frac{E(m, \lambda)}{E(m, \lambda_{ref})} = \left(\frac{\lambda_{ref}}{\lambda} \right)^\beta, \quad (6)$$

where λ_{ref} is a reference wavelength and $E(m, \lambda_{ref})$ is the corresponding $E(m)$ value. It is noticed that these reference values are not explicitly required in the determination of β from the ratio of $E(m)$ values at two wavelengths since they simply cancel out in such ratio. The exponent β is introduced to quantify the spectral variation of $E(m)$. The special case of $\beta = 0$ indicates the highest degree of soot maturity (i.e., no spectral dependence over the range of considered wavelength) whereas $\beta > 0$ means that $E(m)$ decreases with increasing wavelength and the soot can be considered to contain a certain amount of organic compounds. Therefore, β can be used to quantify the degree of soot maturity and will be termed maturity coefficient. Unfortunately, as explained in Section 1, it is very difficult to differentiate graphitic from amorphous soot for the non-organic components of soot material based only on the spectral variation of the absorption function ratio. This is due to the fact that the variation in graphite and amorphous contents essentially affects only the absolute value of $E(m)$ but not its spectral dependence, as shown by Bescond et al. [40]. These authors determined the spectral dependence of the refractive index of different types of carbon nanoparticles in aerosol phase and found three reference materials for which a mixing law can explain the observed variability of the refractive index of any type of soot particles. They found that the soot sampled from an ethylene diffusion flame presents the optical properties of classical graphitic/mature soot, while the soot generated by a miniCAST under certain conditions could exhibit the optical properties of nascent soot or NOCs. Finally, they considered the spark-discharged particles (PALAS GFG) to be representative of pure amorphous carbon as far as the optical properties are concerned.

They provided data and methodology to correlate the spectral dependence of the refractive index and thus $E(m)$ of any soot composed of known components of Organic/Graphitic/Amorphous carbon (expressed in respec-

tive volume fractions). This approach has been used in the present work to determine β based on the amount of organic compounds by assuming a given proportion of amorphous and graphite carbon in the non-organic part. In the present case, we assume that soot particles are composed of organic carbon and graphite carbon components only, i.e, without amorphous carbon. Also, we determine β as the best fit parameter to minimize deviations of the three theoretical ratios of $E(m)$ from the experimentally determined ones, namely $E(m, 810)/E(m, 500)$, $E(m, 810)/E(m, 532)$ and $E(m, 810)/E(m, 660)$. It is noticed that each pair of $E(m)$ ratio is related to the two wavelengths and β through Eq. 6. The variation of β determined by this method with the percentage of organic content is reported in Fig. 2. Also plotted in this figure are the $E(m)$ values at 532 and 810 nm as determined by Bescond et al. [40]. As can be seen, β increases monotonically from $\beta \sim 0.22$ at no organic compound content (pure graphite) up to $\beta \sim 1.20$ for pure organic material. The absorption function $E(m)$ at 532 nm is about 10 to 20% higher than that at 810 nm, depending on the organic carbon content. The $E(m)$ values at both wavelengths decrease monotonically with increasing the organic compound content.

2.4. Soot volume fraction

Once the spectral and spatial dependence of $E(m)$ and the scattering-to-absorption ratio α_λ are determined, the soot volume fraction f_v can be obtained according to Eq. 7,

$$f_v = \frac{k_{ext}\lambda}{6\pi E(m, \lambda)(1 + \alpha_\lambda)}. \quad (7)$$

The proposed methodology has been validated based on numerically simulated extinction and emission signals generated from modeled soot temperature and volume fraction distributions using the CoFlame code. Details of the validation are provided in the Appendix.

3. Experimental apparatus

Fig. 3 shows a schematic of the experimental setup for the absorption/emission measurements. The present study is performed on a canonical non-smoking laminar axisymmetric coflow ethylene-air diffusion flame established on a Gülder type burner at atmospheric pressure. It consists of a 10.9 mm inner diameter central tube for fuel injection, surrounded by a 90 mm inner

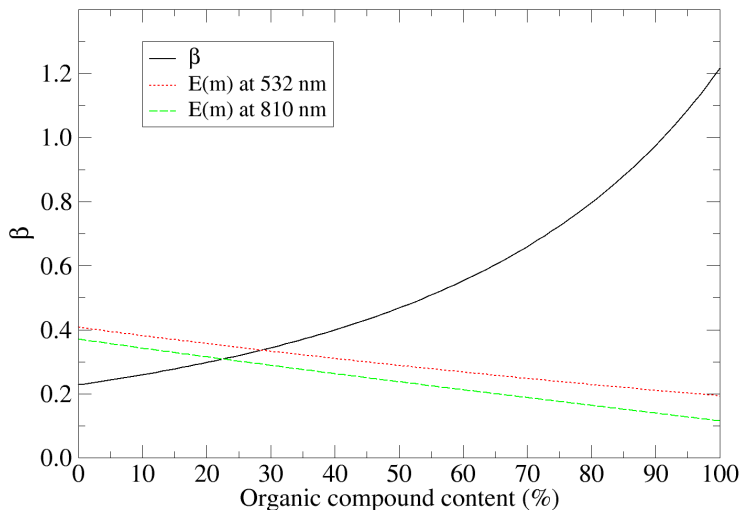


Figure 2: Relationship between the maturity coefficient β and absorption functions $E(m)$ at 532 and 810 nm and the content of organic material in soot particles expressed as volume percentage.

diameter co-annular tube used to supply the coflow air [54]. Two mass flow controllers (Brooks SLA5800 series) were used to deliver constant flow rates of pure ethylene (at 0.194 slpm) and air (at 284 slpm).

To obtain the 2D extinction and emission images, an experimental campaign of LOSA and emission measurements was performed using the experimental setup shown in Fig. 3. For the LOSA measurements, pulsed LED sources (Thorlabs M505L4, M530L4, M660L4 and M810L4) are coupled to an integrating sphere (Thorlabs IS236A-4) in order to provide a uniform diffused light source. The diffuse light is then collimated into a beam by locating an achromatic lens ($f=300$ mm) between the light source and the flame.

The light beam passing through the flame is converged by a second achromatic lens ($f=400$ mm) and captured by an 1004×1002 px² Andor Luca R CCD camera (14 bits) coupled to a Navitar $f2.8/50$ mm lens. Two neutral density filters (O.D. 0.4 and 0.5) and a set of high-transmissivity (> 90%) band-pass filters (centered at 500, 532, 660 and 810 nm) are used to avoid the camera saturation and to spectrally filter the measured signal, respectively.

The soot-laden medium (i.e., flame) transmissivity (τ_λ) is determined from consecutively extinction (LED on) and emission (LED off) intensity measurements. Consequently, the LED operation is modulated at half the camera acquisition rate (8 Hz). Details of the methodology can be found elsewhere [55]. The LED operation and the camera acquisition are carefully synchronized with an external pulse generator (Quantum 9200+).

Additional measurements of the thermal radiation from the flame (mainly from soot) are obtained when the LED illumination is off. Then, the radially-resolved intensity distribution J of soot emission is determined by solving the radiative transfer equation considering the soot self-absorption effect (for details, see Ref. [56] and Appendix A).

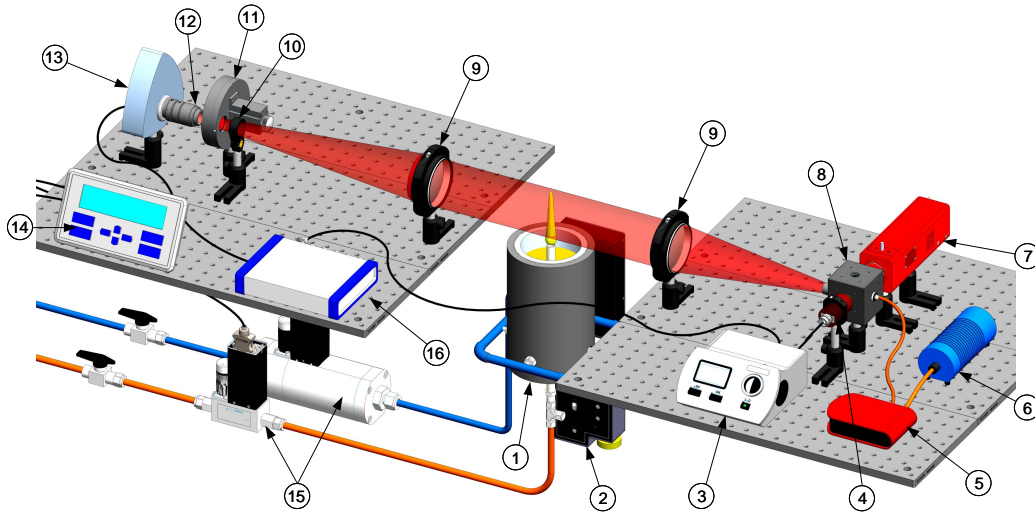


Figure 3: Schematic of the optical rig: (1) burner, (2) translation stage, (3) LED driver, (4) LED source, (5) spectrometer, (6) calibrated light source, (7) stabilized broadband light source, (8) integrating sphere, (9) achromatic lens, (10) neutral density filters, (11) spectral filter wheel, (12) camera lens, (13) Andor CCD camera, (14) mass flow readout module, (15) mass flow controllers, and (16) pulse generator.

In order to improve the signal-to-noise ratio, 150 images were recorded for each detection wavelength ($\lambda = 500 \pm 5$, 532 ± 5 , 660 ± 5 and 810 ± 5 nm), using different exposure times (0.1, 0.06, 0.01 and 0.01 s, respectively). These exposure times improve the signal detection, compensating the exponential increase in the soot emission signal toward the infrared wavelengths.

The detection system linear response was duly verified with a stabilized

tungsten-halogen lamp source (Thorlabs SLS201L/M) by taking light emission images with different exposure times for each wavelength used. These images were also employed to evaluate the global transmissivity of the detection system considering all the optical rig for each detection wavelength (see Fig. 3). For this purpose, the signals captured by the Andor CCD camera were compared with the intensity emitted by the calibrated tungsten-halogen lamp source. Indeed, the spectral response of the CCD camera for each wavelength must be proportional to the spectral emission of the calibrated source affected by the global transmissivity of the detection system. A relative radiometric calibration was carried out using a traceable NIST light source and a spectrometer (Ocean Insight HL-3P-CAL and STS-VIS).

The LOSA and emission experimental signals (τ_λ, P_λ) were deconvoluted in order to obtain the radially-resolved 2D fields of the extinction coefficient k_{ext} and flame emission rate J . The methodology described in Ref. [56] was used in order to account for the self-absorption effects on flame emission. The deconvolution procedure was performed following an onion-peeling method with zero-order Tikhonov regularization [57, 58], where the regularization parameter was selected using the L-Curve criterion [59]. According to this procedure, a regularization parameter of 10^{-5} was determined for the inversion procedure, minimizing the deconvolution error in the flame centerline region but without excessively smoothing the region of large gradients.

4. Results

In this section, the methodology for the determination of soot maturity from a set of four LOSA $k_{ext}(r, z, \lambda)$ and emission rate $J(r, z, \lambda)$ measurements, as defined in Eq. 1 at 500, 532, 660 and 810 nm, is applied to the Gülder ethylene diffusion flame. A prior meticulous and comprehensive numerical analysis has been performed in order to demonstrate the ability of the proposed methodology to extract relevant and accurate information. This numerical validation relies on the predicted soot temperature and volume fraction distributions obtained from a simulation with the CoFlame code [60] and is described in the Appendix. The flame simulation and virtual image generation are described in Appendix A and the proposed methodology is applied to the simulated flame in Appendix B showing its ability and robustness for the retrieval of the local soot volume fraction, temperature, and maturity under typical flame conditions.

It is worth pointing out that the robustness of the Abel inversion algorithm is also reported in [Appendix C](#). Finally, a sensitivity analysis based on a Monte-Carlo approach is summarized in [Appendix E](#), which enables the evaluation of uncertainty propagation and thus provides an estimate of the uncertainty of parameters cited in the discussion below.

4.1. Soot temperature

The emission calibration constant γ is determined according to the methodology described and validated in [Appendix B](#). It is shown that the emission calibration constant can be determined based on the fact that the temperature profiles obtained by the J/k_{ext} approach at 660 and 810 nm along the centerline should be the same.

In the application of the methodology, the temperatures determined from J/k_{ext} (reported in the bottom row of [Fig. 4](#)) are slightly lower than those determined by the 2-color pyrometry technique (the upper row). By comparing the results of the two methods, we observe a different location of the maximum temperatures in the flame wing region though the temperatures from the two methods are overall similar. The shift in the peak temperature location is caused by the rapid evolution of soot maturity, and hence also $E(m)$, in this region, as will be explained later in this section. The temperature distribution derived by J/k_{ext} at $\lambda = 810$ nm does not depend on an assumed value of $E(m)$ and is essentially not affected by scattering effect on extinction at this fairly long wavelength. For these reasons, this temperature distribution will be considered as the exact one in this study. At $HAB = 42$ mm, which is considered a reference height for this flame, the measured temperature is 1580 K at $r = 0$ mm, and 1680 K at $r = 2.25$ mm. These values are respectively 70 K and 150 K lower than those reported in [\[32\]](#). Also at this HAB and $r = 0$, it is 170 K lower than the CARS measurements [\[61\]](#). However, the present results are in very good agreement with the more recent results reported by Rabello de Castro and Figueira da Silva [\[62\]](#) in terms of both profiles and amplitudes. Moreover, de Castro and da Silva reported temperature uncertainties up to 180 K at the same HAB based on 2-C pyrometry. Considering the range of uncertainties, the present temperature results can be considered in overall good agreement with those previously reported in the literature for this flame.

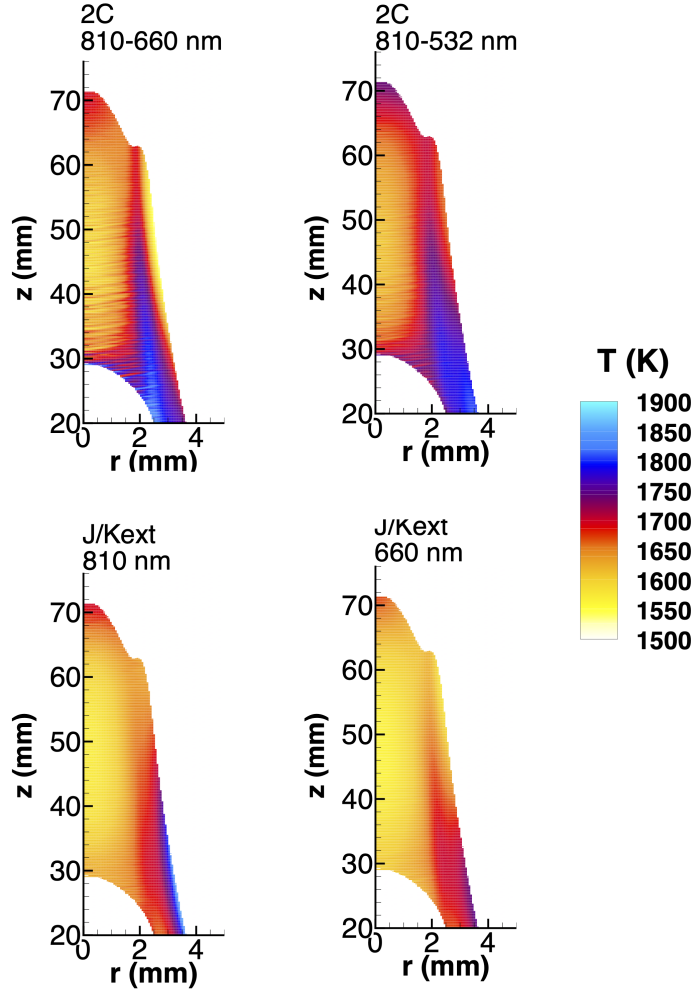


Figure 4: Temperature distributions retrieved from experimentally acquired LOSA/emission images using the 2-color method (top row) and the method proposed in this study (bottom row).

4.2. Soot maturity and composition

Based on the retrieved temperatures and ratios of emissions at different wavelengths, the ratios of $E(m)$ are determined (see Fig. D.13 in Appendix D) through the application of Eq. 5. As illustrated numerically in Appendix B, the 3 determined ratios of $E(m)$ can be used to determine the spectral dependence of $E(m)$ in terms of the maturity coefficient β through best fit.

The results are reported on the left plot of Fig. 5. The high degree of soot maturity (smallest β values) is found near the flame tip in the centerline region (at the top of the flame) and along the flame wing (the outer edge of flame in the radial direction). On the contrary, low level of soot maturity (highest β values) appears at the bottom of the flame corresponding to the presence of nascent and young soot. Indeed, this soot maturity distribution is consistent with our understanding of soot formation processes in laminar coflow diffusion flames. Leschowski et al. [33] determined a maturity ratio based on the comparison of volume fractions measured by LII and light extinction in the same flame in the HAB range between 35 and 42 mm. A direct quantitative comparison between our results and theirs is not straightforward. Nevertheless, the overall distributions of soot maturity are similar: soot maturity level is high along the outer edge of flame wing (the present results) versus higher maturity ratio along the flame wing (their results). Second, with the exception of the flame tip region, the present results show that the soot maturity levels along the flame wing remain higher than those in the centerline region; however, their maturity ratios in the centerline region tend to be higher than those in the flame wing at HAB between 35 and 42 mm.

It is important to mention that the uncertainty associated to β is only ± 0.2 (see Appendix E). Clearly, β appears to be an interesting and useful indicator of the level of soot maturity; however, it is not directly quantitative and intuitive. In order to interpret β more quantitatively and intuitively, we prefer to associate the value of β to the underlying organic carbon volume fraction based on the work of Bescond et al. [40] and illustrated in Fig. 2.

Based on the retrieved distribution of soot maturity coefficient β shown in the left plot of Fig. 5 and the results shown in Fig. 2, soot of high organic carbon content (high values of β) is found at the bottom of the flame in a region of very low volume fractions, which certainly corresponds to nascent soot resulting from the coalescence of large PAHs and also perhaps young soot (nascent soot with limited surface growth). Highly mature soot particles (very low β values) are found in two distinct regions: the top of the flame where oxidation process is intense (soot particles are fully oxidized so the flame is non-smoking) and temperatures are elevated, and in the outer edge of the flame wing where soot volume fractions are relatively high and soot particles undergo intense surface growth through the hydrogen-abstraction acetylene addition (HACA) mechanism and also oxidation by O_2 and OH . It is interesting to notice a shift between the the maximum volume fraction zone marked by the black dashed lines and the region of mature soot (lowest

β values), i.e., the latter is located slightly outside the former in the radial direction. As for the mature soot at the top of the flame, the location coincides with the high temperature zone in the flame centerline region according to the temperature distribution determined by the J/k_{ext} approach (see Fig. 4). It can be seen from this figure that mature soot particles identified along the outer edge of the flame wing region also experience higher temperatures. Temperature is believed to play an important role in the soot maturation process, in particular in graphitization of the material [35]. We will examine next how soot maturity is correlated to the particle size.

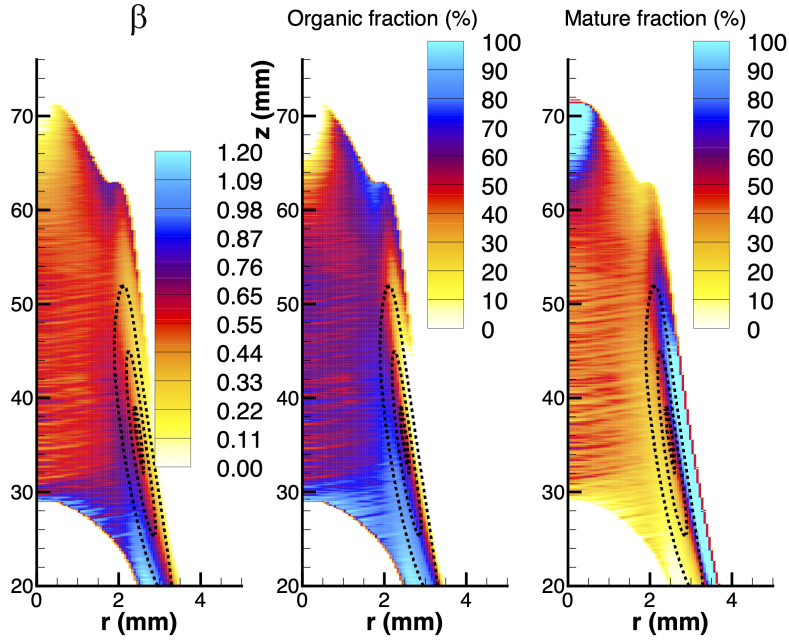


Figure 5: Retrieved distributions of the soot maturity coefficient β and the corresponding to organic and mature (graphitic) soot contents in the laminar coflow ethylene/air diffusion flame based on experimental measurements. The black dashed lines indicate the iso-values of extinction coefficient at 810 nm to help locate the sooting region.

4.3. Scattering contribution

Since the soot temperature has been determined, the contribution of total scattering to the measured extinction can be evaluated based on emission and

LOSA images for each wavelength as given in Eq. 4. These results are shown in Fig. 6 in terms of the scattering-to-absorption ratio. As a comparison, Migliorini et al. [63] evaluated this parameter in the same burner at HAB = 42 mm, $r = 0$ mm, and $\lambda = 532$ nm to be ≈ 0.09 , which is in very good accordance with the currently evaluated value of $\alpha = 0.06$ at the same location. It is evident from Fig. 6 that scattering has significant contributions to extinction at the bottom of the sooting region (where organic materials have a high scattering efficiency), at the flame top in the centerline region, and along the outer edge of the flame wing. The scattering-to-absorption ratio displays the highest values up to about 0.5 along the outer edge of the flame wing, which coincides with the region of mature soot along the flame wing. In the regions of mature soot, the significant contribution of total scattering to extinction can naturally be explained by larger soot particle sizes (primary sphere size plays an important role but also the aggregate size). This suggests that soot particle growth and maturation primarily takes place along the outer edge of the flame wing and with a slight shift radially outward relative to the high soot volume fraction zone (see profiles extractions in Fig. 6). This growth and maturation process is more pronounced at the lower and middle parts of the flame wing, which are the hottest regions of the flame. The radial gradients of the soot maturity coefficient are very high, suggesting that the soot maturation process is highly dependent on the thermal and chemical conditions.

4.4. Soot absorption function and volume fraction

Finally, the soot maturity coefficient β is used to determine the absolute $E(m)$ at 810 nm (see Fig. 2). The $E(m, 810)$ value is obtained with an uncertainty estimated at ± 0.07 (please see Appendix E). The absorption function is required to convert the LOSA data at this wavelength to soot volume fraction (see Eq. 7). The results are reported in Fig. 7 and a sensitivity analysis found that f_v has an uncertainty of ± 2.3 ppm (see Appendix E). As expected, the derived $E(m, 810)$ distribution in the right plot of Fig. 7 correlates precisely with the soot maturity coefficient β : higher $E(m)$ value region corresponds to higher soot maturity or higher content of graphitic soot. Based on the left plot of Fig. 7, it is very important to take into account the spatial variation of soot optical properties characterized here by $E(m)$ in the present context, i.e., in the determination of soot volume fraction from the local absorption coefficient. This is revealed by a slight shift in the location of peak soot volume fraction toward the flame centerline com-

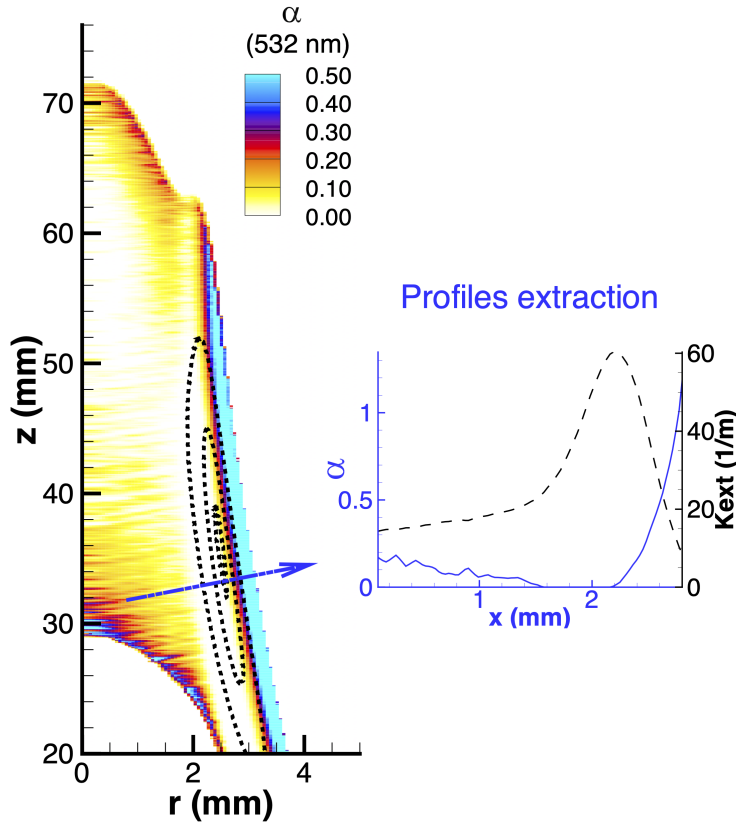


Figure 6: Contribution of soot scattering to extinction measurement at $\lambda = 532$ nm. The black dashed lines display the iso-values of extinction coefficient at 810 nm in order to locate the soot volume fraction region. The inset presents the extracted profiles along the blue dot-dash line. The black dashed curve displays k_{ext} measured at 810 nm and the blue solid curve shows α determined at 532 nm.

pared to the peak extinction coefficient (black dashed lines, at 810 nm the extinction coefficient can be considered the same as absorption coefficient) in the left plot. The slight shift in the locations of peak soot volume fraction and peak extinction coefficient is caused by the generally neglected strong spatial variation in $E(m)$ induced by the soot maturation process. The importance of considering the spatial variation of soot $E(m)$ in soot volume fraction determination using the extinction measurement at 810 nm can be

better highlighted by comparing the soot volume fraction distributions along the blue dot-dash line by assuming a constant $E(m) = 0.37$, which is the value of mature soot at 810 nm (Tab. B.1, the black dashed line in the inset) and by using the spatially varying $E(m)$ shown in the right plot of Fig. 7 (solid blue line in the inset). The shift in the location of the maximum f_v is clearly observed in the inset as well as the significant underestimation of f_v when considering a constant $E(m)$. It is interesting to notice that the volume fraction profile obtained with the hypothesis of a constant $E(m)$ (black dash line) provides results in very good agreement with previously reported data, e.g. by Thomson et al. [64] even though their flame is slightly smaller. Also, we can notice that the present evaluation of soot volume fraction is in excellent agreement with previously reported values at HAB = 42 mm in the centerline. Indeed, the 4.5 ppm obtained in this study is identical to Snelling et al. [54] and in the range of reported values (3.9 to 5 ppm) reviewed by Schulz et al. [65]. Nevertheless, it can be noticed that Leschowski et al. [33] reported a lower volume fraction at the same position (about 2.4 ppm) determined by the Auto Compensated LII method.

5. Conclusion and perspectives

A methodology for accurate determination of soot temperature, volume fraction, and maturity in laminar axisymmetric coflow flames using multi-wavelength attenuation and emission measurements was developed and demonstrated. The ability to fully characterize soot properties is crucial for improving our understanding of soot particles formation and maturation processes in flames. Comprehensive and high-quality experimental dataset of soot parameters is highly desirable for validating robust soot models that are indispensable for the design of future cleaner combustion devices.

Up to now, the two-color emission method has been commonly used to infer soot temperature based on the hypothesis of a constant, both spectrally and spatially, soot absorption function. However, even a weakly spectral dependence of soot absorption function can produce a fairly large error in the measured temperature. In the present study, the ratio of emission and extinction is shown to be significantly more accurate because it is independent of *a priori* assumption of the absorption function. In addition, spectrally-resolved emission and LOSA measurements were conducted to derive the soot maturity coefficient that reveals the local soot composition in terms of the volume fractions of organic carbon and graphitic carbon. This knowledge

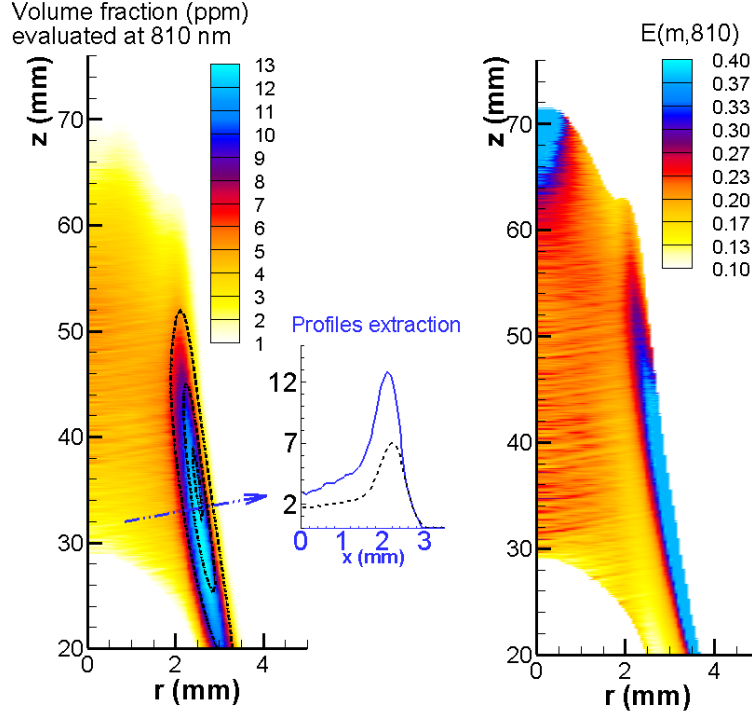


Figure 7: Distributions of the absolute $E(m)$ at $\lambda = 810$ nm (right plot) and the corresponding soot volume fraction (left plot). Black dashed lines show the iso-values of extinction coefficient at 810 nm. The inset shows the f_v profiles along the blue dot-dash line using a constant $E(m) = 0.37$ (black dashed line) and the spatially varying $E(m)$ (solid blue line).

is particularly informative concerning our understanding of the soot formation processes. In particular, this study reveals the strong gradients of soot maturity in the outer edge of the flame wing, which seem correlated with the high-temperature region where soot particles undergo strong surface growth and oxidation. Based on the hypothesis that the soot maturity is a result of the graphitization/dehydrogenation process (without considering the impact of the oxidation step in the present study), the soot maturity coefficient introduced in this study is related to the absolute absorption function, enabling a more accurate determination of soot volume fraction using spatially dependent soot absorption function, instead of assuming a constant value throughout the flame. Although this consideration only slightly shifts the

location of peak soot volume fraction, it can strongly affect the values of soot volume fraction in certain regions.

The robustness and consistency of the technique was tested using numerically generated transmission and emission images based on predicted soot temperature and volume fraction distributions from the CoFlame code. The relative error in the determination of the absorption function and soot volume fraction is considered less than about 10%. The applicability of this technique is currently limited to 1D or 2D axisymmetric flames. It thus can be readily adapted to study such laminar sooting flames. It is planned to apply this technique to study the influence of fuel composition on the soot formation processes. Other parametric studies are also envisaged in order to understand certain phenomena such as the flame opening and the related soot emission processes. Finally, the technique developed in this study will be used to obtain comprehensive experimental dataset for validation of soot formation models.

Acknowledgments

The authors gratefully acknowledge the support provided by France's ANR ASTORIA under the research grant ANR-18-CE05-0015 and the Region of Normandy RIN Gaspropres project and Chile's National Agency for Research and Development (ANID) through research program Fondecyt/Regular 1191758. Also, this work was performed by the mobility France-Chile joint program receiving a research grant provided by Ecos/ANID C19E01.

Appendix A. Flame modeling and generation of synthetic signals

Appendix A.1. Flame model

Numerical simulations were performed for the purpose of validating the proposed methodology for determining the distribution of soot maturity in terms of the maturity coefficient β . The CoFlame code [60, 66–68] was used to simulate a laminar axisymmetric coflow ethylene/air diffusion flame established on a Gülder type burner [54]. This flame code models axisymmetric flames using detailed gas-phase combustion chemistry and including all known physical and chemical processes involved in soot chemistry and dynamics. The code solves the conservation equations for mass, momentum, species mass fractions, energy and the population of soot particles. A fixed sectional method [66] is used for solving the population balance equation of soot particles in terms of the number density of soot aggregates (N_{agg}) and primary particles (N_{pp}), where the mass range of soot particles is logarithmically divided into 35 discrete sections. The spacing factor between sections is chosen adequately to ensure that N_{agg} and N_{pp} vanish in the last section, i.e., to ensure that the largest soot particles in the flame are resolved. The flame chemistry is modeled by using the chemical mechanism developed at the German Aerospace Center (DLR) [69] with the modifications proposed by Dworkin et al. [70]. The soot formation model considers nucleation of soot particles from the collision of the 3 heaviest polycyclic aromatic hydrocarbons (PAHs) in the chemical mechanism, namely benzo[a]pyrene (BAPYR), secondary benzo[a]pyrenyl (BAPYR*S) and benzo(ghi)fluoranthene (BGHIF). The same PAHs are used for modeling PAH condensation onto soot particle surface. In addition to PAH condensation growth, the model also includes soot particle surface growth and oxidation reactions via the hydrogen-abstraction carbon-addition (HACA) mechanism [71]. Moreover, particle coagulation, oxidation-induced fragmentation, and thermophoresis are also considered. The radiative source term in the energy equation is obtained by solving the radiative transfer equation (RTE) using the discrete ordinates method [72] coupled with a statistical narrow-band correlated-k model for the absorption coefficients of CO, CO₂, H₂O, and soot [73]. Further details of the numerical model can be found in [60].

Appendix A.2. Numerical details

The computational domain for the simulation of laminar coflow ethylene/air diffusion flame starts at the fuel tube exit along the streamwise

direction; thus, the flow inside fuel tube and heat transfer between the flame base and the fuel tube are not modeled. A non-uniform numerical grid is used, which consists of 202 (axial, z) \times 94 (radial, r) control volumes (CVs) extending to 14.3 cm and 2.74 cm, respectively. The mesh size remains constant at 0.02 cm (r) \times 0.05 cm (z) in the near burner region to capture the steep gradients and becomes coarsened at a constant stretching factors of 1.05 outside this region in both the streamwise and radial directions. Pure ethylene is injected through the central tube of the burner at 3.465 cm/s and ambient air (assumed as mixture of 21%O₂ and 79%N₂) is injected through the co-annular region between both concentric tubes at 61.255 cm/s. Flat velocity profiles are imposed at both the fuel and air inlets. Both the fuel and air are delivered to the burner at 300 K and atmospheric pressure. The converged simulation under these conditions produced a stable, non-smoking flame of approximately 7.2 cm visible flame height, providing detailed distributions of soot volume fraction f_v and gas-mixture temperature T (equal to soot temperature T_s under the assumption of thermal equilibrium), as well as all other thermal and chemical variables included in the CoFlame code.

Appendix A.3. Absorption and scattering coefficients

The CoFlame simulation provides detailed properties of soot particles, such as soot volume fraction, diameter of primary particles composing a soot aggregate (d_p), number density of aggregates and primary particles, average number of primary particles per aggregate $n_p = N_{pp}/N_{agg}$, and soot temperature, among others. These properties are sufficient to compute the absorption and scattering coefficients of soot particles through the Rayleigh-Debye-Gans (RDG) approximation [74]. For this approach, soot particles are assumed to be fractal aggregates composed by a number of spherical primary particles ($n_p = N_{pp}/N_{agg}$) that are in point-contact, following the statistical scaling relationship

$$n_p = k_f(2R_g/d_p)^{D_f} \quad (\text{A.1})$$

where R_g is the gyration radius, $k_f = 2.3$ and $D_f = 1.78$ are the fractal pre-factor and fractal dimension, respectively [74]. Soot aggregates are considered to be monodisperse. With this approach, the absorption (C_{abs}) and scattering (C_{sca}) cross sections of soot aggregates can be determined by assuming a model for the functions $E(m)$ and $F(m)$ (see Table B.1). The soot absorption (k_{abs}) and total scattering (k_{sca}) coefficients are calculated as:

$$k_{abs,\lambda} = C_{abs}N_{agg}, \quad \kappa_{sca\lambda} = C_{sca}N_{agg} \quad (\text{A.2})$$

which allows to compute the contribution of total scattering to extinction in terms of the scattering-to-absorption ratio α_λ . For further details, please see [74, 75].

Appendix A.4. Generation of synthetic transmission and emission signals

The numerically predicted values of f_v and T in the laminar coflow ethylene/air diffusion flame allows the generation of synthetic images simulating the line-of-sight signals captured by cameras in LOSA and flame emission measurements. Applying the Abel inversion to these synthetic images permits the retrieval of spatially-resolved f_v and T . Then, a direct comparison of the reconstructed values f_v and T obtained from the synthetic images with the CoFlame predicted f_v and T , which are used to generate the synthetic signals, serves as validation and self consistency assessment of the proposed methodology. Although this self consistency check seems simple and straightforward, it is important and necessary to validate the methodology before applying it to the experimental images of transmission and emission obtained at the four wavelengths to reconstruct soot temperature, volume fraction, $E(m)$, and soot maturity coefficient.

The LOSA technique is based on the assumption that the light propagating through the flame is absorbed and scattered only by soot particles within the flame, which is valid for detection in the visible and near infrared below 1000 nm wavelength at flame temperatures (typically less than about 2300 K).

The ratio of the detected light intensity to the source intensity, i.e., the transmissivity, can be expressed as:

$$\tau_\lambda = \exp \left(- \int_{l_0}^{l_1} k_{\text{ext},\lambda}(l) dl \right) \quad (\text{A.3})$$

where l_0 and l_1 indicate the start and end points, respectively, of the section of light intercepted by the flame along the optical path between the source of light and the camera, and the subscript λ denotes wavelength dependence. By selecting a wavelength λ and the corresponding value of the absorption function $E(m, \lambda)$, we can use the simulated values of f_v , α_λ and Eq. 1 to obtain the simulated values of $k_{\text{ext},\lambda}$. Then, through numerical integration of Eq. A.3 over all possible parallel line-of-sight cords covering the visible flame cross-section at a given height it is possible to generate synthetic transmission images simulating the transmission signal captured by the camera $-\ln(\tau_\lambda)$.

In a similar way, the line-of-sight integrated flame emission captured by a photodetector (P_λ) can be modeled through the solution of the RTE (see [56] for further details):

$$P_\lambda = \int_{l_0}^{l_1} k_{\text{abs},\lambda}(l) B_{T,\lambda}(l) \exp\left(-\int_l^{l_1} k_{\text{ext}}(l') dl'\right) dl \quad (\text{A.4})$$

where self-absorption, including the effect of scattering, was taken into account. With the simulated values of T we can compute the Planck's function $B(T, \lambda)$ at a selected λ . Then, with the predicted f_v and an assumed soot $E(m)$ model $k_{\text{abs},\lambda}$ is readily known and it is possible to compute a synthetic convoluted emission signal P_λ through numerical integration of Eq. A.4 to simulate what would be captured by a photodetector experimentally.

The simulated values of $k_{\text{abs},\lambda}$, τ_λ , T , $B(T, \lambda)$ and P_λ serve as a reference for testing and validating the proposed methodology, as presented later in [Appendix B](#) and [Appendix C](#).

Appendix B. Demonstration of the methodology using numerically simulated signals

This section aims at showing the different steps of data processing and to demonstrate its robustness for retrieval of the local soot volume fraction, temperature, and maturity under typical flame conditions. To create a challenging situation to test the robustness of the methodology, the simulated flame is arbitrarily divided into two distinct zones separated at $HAB = 40$ mm and the soot particles are supposed to be made of pure organic and graphitic carbon below and above this HAB , respectively. The corresponding absorption functions at the four wavelengths used for the generation of synthetic LOSA and emission images are reported in Table B.1 for each wavelength and the two zones, i.e., below and above $HAB = 40$ mm, as well as the three pairs of $E(m)$ ratio. The corresponding $F(m)$ used for the evaluation of the scattering contribution is also reported in the table.

Table B.1: The $E(m)$ and $F(m)$ values of organic and graphitic carbon at the four wavelengths and the ratios of $E(m)$ of three pairs of wavelength (based on Bescond et al. [40])

	Organic	Graphitic
$E(m,500)$	0.22	0.42
$E(m,532)$	0.19	0.41
$E(m,660)$	0.14	0.38
$E(m,810)$	0.12	0.37
$E(m,810)/E(m,660)$	0.81	0.97
$E(m,810)/E(m,532)$	0.60	0.91
$E(m,810)/E(m,500)$	0.54	0.89
$F(m,500)$	0.31	0.33
$F(m,532)$	0.29	0.34
$F(m,660)$	0.26	0.36
$F(m,810)$	0.23	0.40

Fig. B.8 compares the flame centerline temperature distributions determined by the 2-color approach (Eq. 2) and by the proposed method based on the ratio J/k_{ext} (Eq. 3), as well as with numerically predicted distribution by the CoFlame code. It is noticed that the spectral dependence of $E(m)$ was neglected in the 2-color approach. We can observe clearly that the recovered local temperature is strongly influenced by the deviation of $E(m)$ ratio from

unity, which was assumed in the 2-color approach. Even for the pair of the two longest wavelengths of (660-810 nm), which are also not too far apart, and graphitic soot (at HAB > 40 mm and for which $E(m, 810)/E(m, 660) = 0.97$) the 2-color approach consistently overestimates the input temperature from CoFlame by more than 50 K. We observe a much larger discrepancy at the bottom of the flame below HAB = 40 mm, where soot is assumed to be made of organic carbon and the $E(m)$ ratios are significantly lower than unity, the 2-color approach significantly overestimated soot temperature. To obtain the temperature based on J/k_{abs} (Eq. 3) the calibration constant γ has to be determined. The proposed methodology consists in searching for the value of γ leading to identical temperature profiles at 810 and 660 nm. This enables an exact temperature to be determined. In this context, the temperature determined based on J/k_{abs} at 810 nm resulting from this iterative procedure is used for further computations.

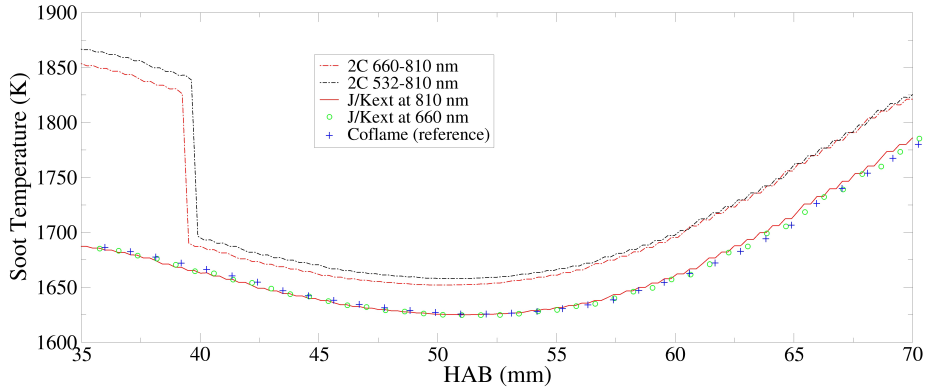


Figure B.8: Comparison of the recovered flame centerline temperatures distributions by the 2-color approach and the proposed method with the result by CoFlame simulations.

Fig. B.9 shows the determined ratios of $E(m)$ based on Eq. 5 for the simulated flame. First, regardless of the flame location (associated with different local soot volume fraction, scattering contribution, self-absorption of flame emission and temperature), these ratios are almost uniform within the prescribed two zones of organic and graphitic soot separated by HAB = 40 mm, and the retrieved ratios are in good agreement with those imposed in the generation of synthetic images (see Table B.1). The so determined ratios are found to be slightly smaller (between 3 and 7%) than those used for images

generation, especially for distant pairs of wavelengths and for the region of organic carbon. This slight discrepancy is due to the scattering contribution and self-absorption of flame emission. Indeed, when synthetic images are generated without considering those effects, the ratios of $E(m)$ are perfectly found. In consequence of this analysis, in a typical laminar axisymmetric flame environment, determining the $E(m)$ ratios would be *a priori* possible based on multi-wavelength measurements of transmission and emission as shown here.

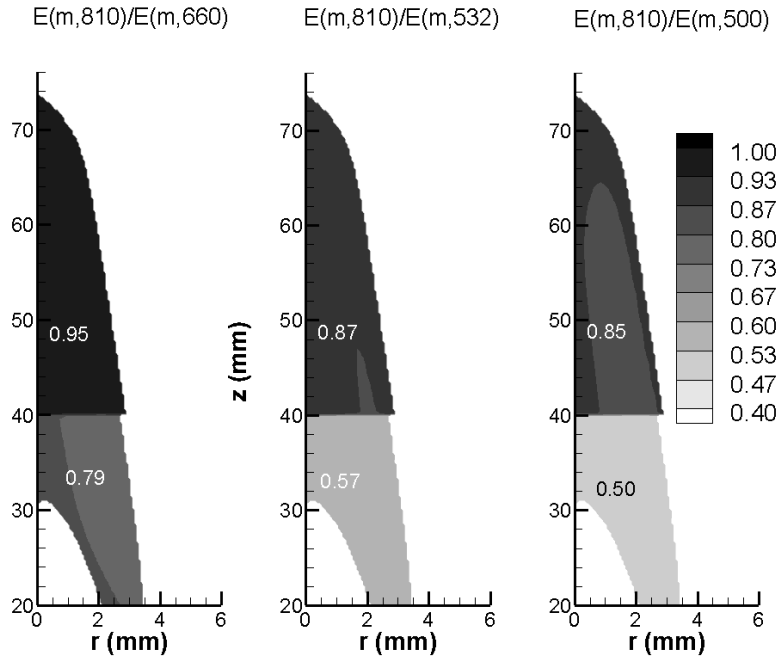


Figure B.9: Distributions of the determined $E(m)$ ratios at three pairs of wavelength based on synthetic images generated from CoFlame simulation.

The next step consists in determining the maturity coefficient β defined in Eq. 6 based on the recovered ratios of $E(m)$ shown in Fig. B.9 through a fitting process. The results are reported in Fig. B.10. As expected, only pure organic carbon is found in the bottom part ($\beta \sim 1.2$, below HAB = 40 mm) and mature graphitic soot ($\beta \sim 0.2$) in the upper part of the flame (above HAB = 40 mm). The region of mature soot is not perfectly uniform

as it should be. This is again caused by the scattering contribution and self-absorption of flame emission, which appears to be not totally removed during the deconvolution process.

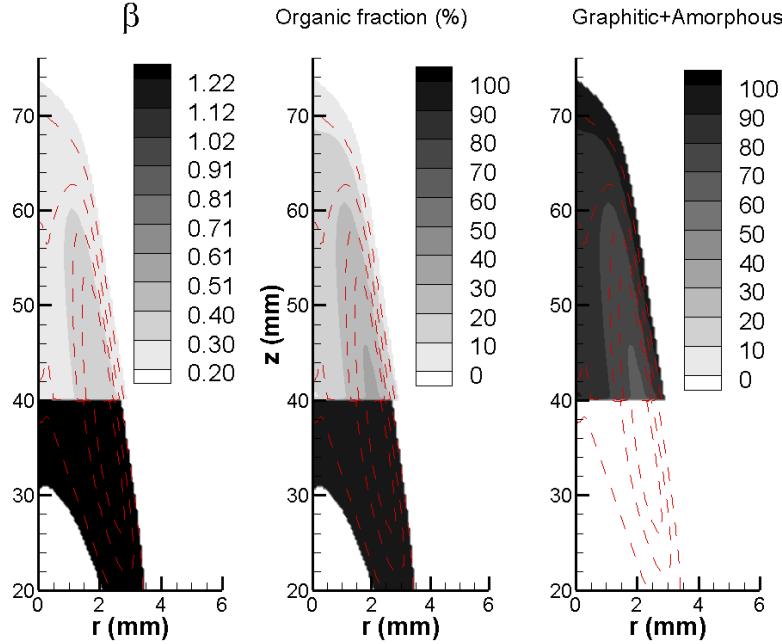


Figure B.10: Distribution of the determined maturity coefficient β and the corresponding organic and mature graphitic soot contents using synthetic images based on CoFlame simulation. Red dash lines represents volume fraction isovalues.

Finally, as shown earlier in Fig. 2, the absolute value of $E(m)$ at a specified wavelength can be obtained once the maturity coefficient β is determined. As an example, the distributions of recovered absolute values of $E(m)$ at 810 nm and the corresponding soot volume fraction are reported in Fig. B.11. In both the organic carbon and graphitic carbon regions, separated at $HAB = 40$ mm, the values of $E(m)$ are properly retrieved in particular in the region of organic soot (see Tab. B.1). In the upper region of mature soot, $E(m)$ is retrieved with a 13.5% underestimation. As previously explained, this is caused by the consideration of the trapping of emitted signal due to self absorption and scattering during the virtual images generation. Also, the retrieved soot volume fraction distribution using Eq. 7 is also found in good agreement with

that predicted by CoFlame and used in generating the synthetic images as input for the data processing of the proposed methodology. We just notice a slight discontinuity at the transition between the two regions that can reach 1.5 ppm. Nevertheless, it must be recalled that a classical determination of the volume fraction based on extinction data interpretation with a constant $E(m)$ set at 0.4 for example would have produced a discontinuity in the volume fraction 3 times larger at the same location.

This section has demonstrated the ability to process the synthetic emission and LOSA images at four different wavelengths using the proposed method to retrieve spatially-resolved soot temperature, volume fraction, maturity coefficient and further the organic and graphitic carbon contents of soot. It is noticed that without considering the contribution of soot scattering to extinction and self-absorption of flame emission (not presented), the inversion process can perfectly recover the input soot temperature and volume fraction distributions.

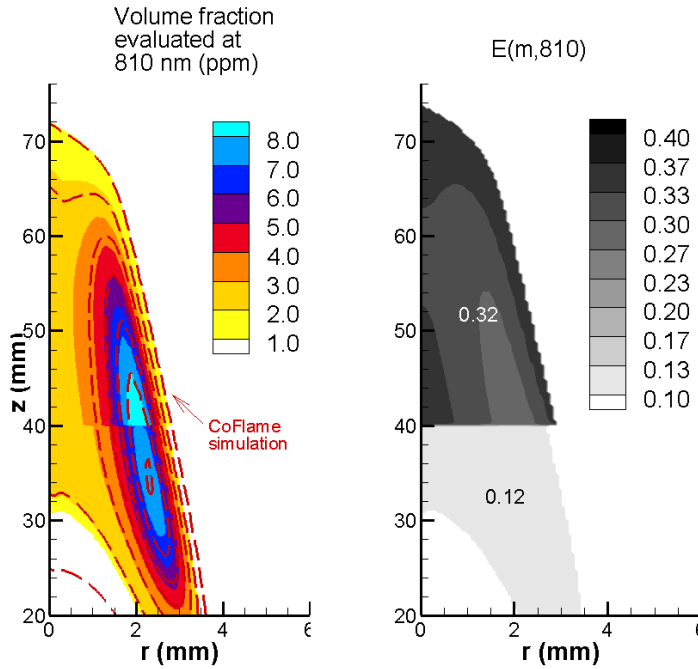


Figure B.11: Evaluation of the absolute $E(m)$ at 810 nm and the volume fraction extraction for the CoFlame simulation.

Appendix C. Robustness and performance of the Abel inversion algorithm

The objective of this section is twofold: to evaluate the robustness of the inversion method with respect to signal noise in the deconvolution step and to compare the sensitivity of the retrieved results to the chosen deconvolution method. To this end, the CoFlame simulation results of f_v and T have been convoluted (without considering self-absorption) to generate the synthetic images of transmission and emission signals as in the last section. Subsequently, a random Gaussian noise between 0 and 1% of the maximum value for the standard deviation is added to each pixel of the synthetic images in order to mimic experimental uncertainties, and finally the noise-added images are deconvoluted using different methods. The same deconvolution method used for experimental images is used (referred to as EC2G Abel) here with a similar regularization parameter (10^{-5}) as used in the deconvolution of experimental images [55]. An alternative method (referred to as PyAbel) is also used from the publicly available PyAbel library by selecting the “Hansenlaw” method [76].

Fig. C.12 reports the retrieved results of the absolute value of $E(m)$ at $\lambda = 810$ nm as well as the corresponding soot volume fraction (taking into account the spatial variation of $E(m)$) using the two inversion methods respectively without and with the scattering contribution considered. Both the $E(m)$ at 810 nm and f_v distributions were well retrieved by both inversion methods, which seem robust in the sense that the noise in the signals did not cause significant noise in the retrieved local values of $E(m)$ and f_v . The two zones of uniform and distinctively different $E(m)$ values are well recovered as well as the region of high volume fractions (region of high gradients of red dashed curves). The deconvoluted results from the EC2G method seem less noisy as indicated by less empty pixels. A quantitative evaluation of the performance of the two inversion methods is reported in Tab. C.2. The performance is expressed in terms of the errors of the retrieved $E(m)$ and f_v values in the regions enclosed by red box in the figure in the two distinct regions in Fig. C.12 and referred as zone G (graphitic) and zone O (organic). The deconvolution process recovers $E(m)$ about 10% lower in both regions (only 2.3% in the O region by EC2G). The added noise results in a standard deviation of the derived $E(m)$ between 17% and 53% with significantly better results (lower error and standard deviation) when using the EC2G Abel method and in the region of mature graphitic soot. Better agreement

is also observed between the retrieved soot volume fraction distribution and that predicted by the CoFlame code. It is useful to recall that unlike $E(m)$, which is imposed to be uniform but has two very different values in the two zones below and above $HAB = 40$ mm, f_v varies continuously in the flame, explaining why larger standard deviations are observed for f_v .

We conclude from this analysis that the retrieved distributions of $E(m)$ and f_v from the inversion procedure display fairly good accuracy even when random uncertainties similar to those found in experiments are added to the synthetic signals in the process of Abel deconvolution. The inversion method used for the experimental signal analysis in the next section (EC2G Abel) retrieves results in good agreement with those from the selected PyAbel method. Based on the above analysis, we can conclude that the global uncertainties of the retrieved local quantities from the inversion process are about 10%, for both $E(m)$ and f_v . It is useful to point out that the relatively lower accuracy of the selected PyAbel inversion method is not necessarily intrinsic to the library, since it was only a simple application of this library in our study without optimization. It is likely that more accurate results can be obtained when the method was used in combination with a data noise reduction procedure [77]; however, it was not pursued in this study.

Deconvolution method	EC2G Abel		PyAbel	
Zone	G	O	G	O
$E(m, 810)$ err. (%)	-10.9	-2.3	-11.9	-13.4
$E(m, 810)$ std (%)	16.9	33.9	23.5	53.2
f_v err. (%)	19.5	-6.9	17.6	-16.6
f_v std (%)	31.4	52.3	46.2	64.2

Table C.2: Relative errors of $E(m)$ at 810 nm and f_v from deconvolution of synthetic images based on CoFlame simulation of the flame with random noise added. The relative errors are computed over the two regions enclosed by the two red boxes in Fig. ??.

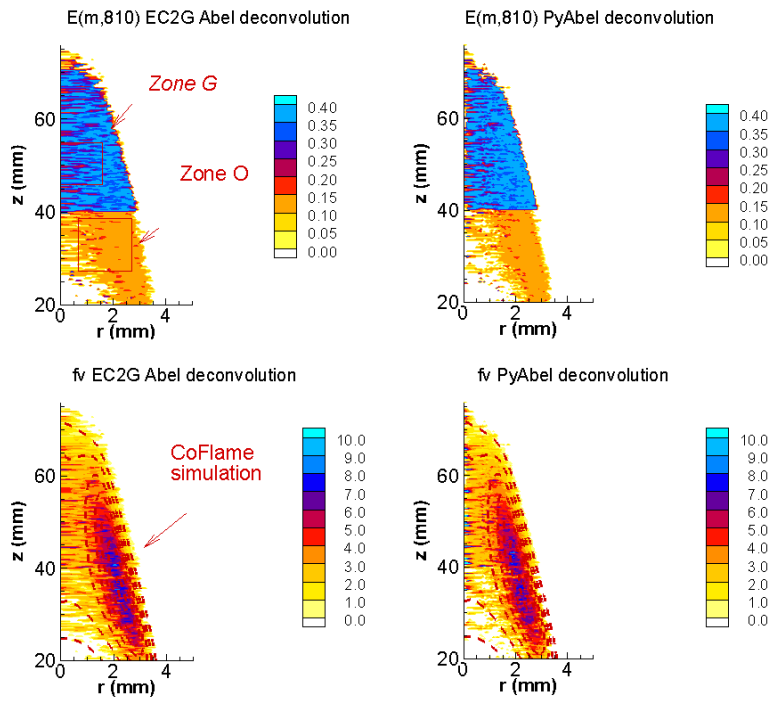


Figure C.12: Impact of the deconvolution method on the retrieved distributions of $E(m)$ at 810 nm and the corresponding soot volume fraction using the synthetic signals based on CoFlame simulation with random noise added. Two deconvolution processes are achieved using EC2G (also used for the experimental data analysis) and PyAbel (Hansenlaw) for comparison.

Appendix D. Ratios of $E(m)$

See Fig. D.13

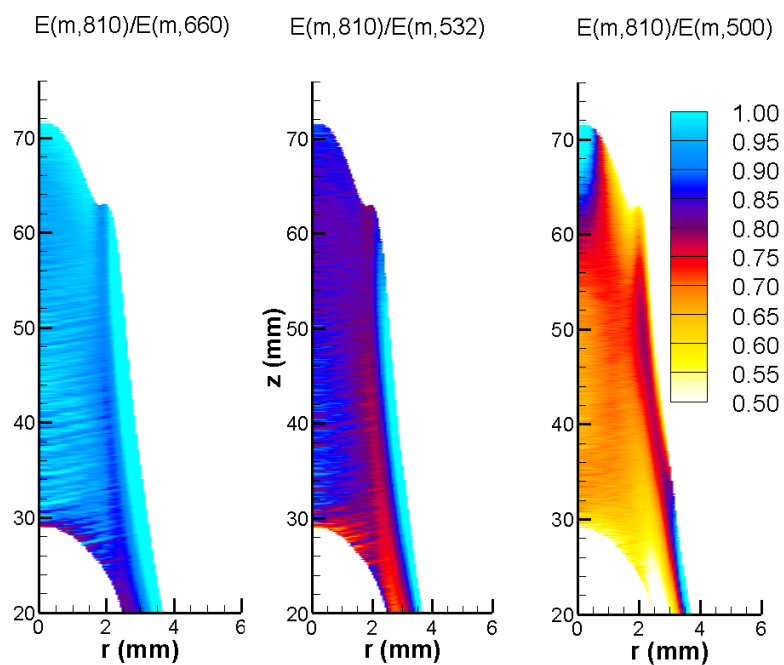


Figure D.13: Retrieved distributions of $E(m)$ ratio at three pairs of wavelength from attenuation and emission measurements at four wavelengths.

Appendix E. Sensitivity analysis of the inversion of measured transmission and emission images

The aim of this appendix is to complement the sensitivity analysis of the synthetic images generated with the CoFlame code, where the methodology proposed and the Abel deconvolution process were properly tested. The purpose here is to test the methodology from an experimental standpoint by carrying out a sensitivity analysis of relevant quantities derived from the extinction and emission measurements at four wavelengths: f_v , $E(m, 810)$, β and T (based on J/k_{ext} at 810 nm).

To this end, the propagation of uncertainties is simulated by employing a Monte-Carlo approach and considering a Gaussian dispersion of each measured signal with a 5% standard deviation for the derived parameters.

The results of relative error are reported in Fig. E.14. The estimated standard deviations are normalized by the corresponding local value along the radial profile at HAB = 46.6 mm.

It can be observed that the evaluation of soot temperature is robust with a small standard deviation of about 12 K. On the other hand, the β parameter presents a different response, since it produces relative errors about 0.4 in regions of low β (mature soot) and up to 0.8 in the regions of large β (nascent soot). This corresponds to an overall uncertainty of about ± 0.2 . Nevertheless, the uncertainties in f_v and $E(m, 810)$ are largely unaffected because both exhibit a relative variation close to 27%. This corresponds to an evaluation for $E(m, 810)$ with an uncertainty of ± 0.07 and for f_v with an uncertainty of ± 2.3 ppm. Finally, the same trends are observed independent of the HAB tested.

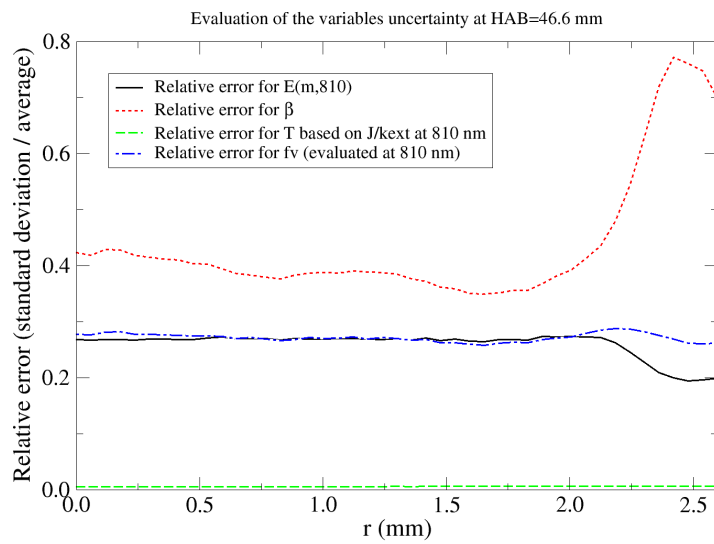


Figure E.14: Radial profiles uncertainties based on a Monte-Carlo error propagation approach at HAB = 46.6 mm.

References

- [1] Z. D. Ristovski, B. Miljevic, N. C. Surawski, L. Morawska, K. M. Fong, F. Goh, I. A. Yang, Respiratory health effects of diesel particulate matter, *Respirology* 17 (2012) 201–212.
- [2] T. C. Bond, S. J. Doherty, D. W. Fahey, P. M. Forster, T. Berntsen, B. J. DeAngelo, M. G. Flanner, S. Ghan, B. Kärcher, D. Koch, et al., Bounding the role of black carbon in the climate system: A scientific assessment, *J. Geophys. Res. Atmos.* 118 (2013) 5380–5552.
- [3] M. Lapuerta, J. Sánchez-Valdepeñas, J. Barba, D. Fernández-Rodríguez, J. P. Andrés, T. García, Analysis of soot from the use of butanol blends in a euro 6 diesel engine, *Energy Fuels* 33 (2019) 2265–2277.
- [4] R. Niranjana, A. K. Thakur, The toxicological mechanisms of environmental soot (black carbon) and carbon black: focus on oxidative stress and inflammatory pathways, *Front. Immunol.* 8 (2017) 763.
- [5] R. Viskanta, M. Mengüç, Radiation heat transfer in combustion systems, *Prog. Energy Combust. Sci.* 13 (1987) 97–160.
- [6] B. Apicella, A. Ciajolo, A. Tregrossi, J. Abrahamson, R. Vander Wal, C. Russo, HRTEM and EELS investigations of flame-formed soot nanostructure, *Fuel* 225 (2018) 218–224.
- [7] R. A. Dobbins, H. Subramaniasivam, Soot precursor particles in flames, in: *Soot formation in combustion*, Springer, 1994, pp. 290–301.
- [8] A. D’Anna, A. D’Alessio, P. Minutolo, Spectroscopic and chemical characterization of soot inception processes in premixed laminar flames at atmospheric pressure, in: *Soot formation in combustion*, Springer, 1994, pp. 83–103.
- [9] T. S. Totton, D. Chakrabarti, A. J. Misquitta, M. Sander, D. J. Wales, M. Kraft, Modelling the internal structure of nascent soot particles, *Combust. Flame* 157 (2010) 909–914.
- [10] C. G. Fernández, S. Picaud, M. Devel, Calculations of the mass absorption cross sections for carbonaceous nanoparticles modeling soot, *J. Quant. Spect. Rad. Trans.* 164 (2015) 69–81.

- [11] H. A. Michelsen, M. Colket, P.-E. Bengtsson, A. D’Anna, P. Desgroux, B. S. Haynes, J. H. Miller, G. J. Nathan, H. Pitsch, H. Wang, A review of terminology used to describe soot formation and evolution under combustion and pyrolytic conditions, *ACS nano* (2020).
- [12] A. Baldelli, U. Trivanovic, T. A. Sipkens, S. N. Rogak, On determining soot maturity: A review of the role of microscopy-and spectroscopy-based techniques, *Chemosphere* (2020) 126532.
- [13] M. Li, F. Bao, Y. Zhang, W. Song, C. Chen, J. Zhao, Role of elemental carbon in the photochemical aging of soot, *Proc. Natl. Acad. Sci. USA* 115 (2018) 7717–7722.
- [14] Y. Han, J. Cao, J. C. Chow, J. G. Watson, Z. An, Z. Jin, K. Fung, S. Liu, Evaluation of the thermal/optical reflectance method for discrimination between char- and soot-EC, *Chemosphere* 69 (2007) 569–574.
- [15] J. G. Watson, J. C. Chow, L.-W. A. Chen, Summary of organic and elemental carbon/black carbon analysis methods and intercomparisons, *Aerosol Air Qual. Res.* 5 (2005) 65–102.
- [16] S. Lim, S. Lee, T. Ahn, S. Park, Measurement of organic carbon content during the growth soot particles in propane normal and inverse diffusion flames using a multi-wavelength light extinction method, *Carbon* 149 (2019) 519–529.
- [17] M. Sirignano, M. Alfè, A. Tregrossi, A. Ciajolo, A. D’Anna, Experimental and modeling study on the molecular weight distribution and properties of carbon particles in premixed sooting flames, *Proc. Combust. Inst.* 33 (2011) 633–640.
- [18] B. Apicella, P. Pré, J. Rouzaud, J. Abrahamson, R. L. Vander Wal, A. Ciajolo, A. Tregrossi, C. Russo, Laser-induced structural modifications of differently aged soot investigated by HRTEM, *Combustion and Flame* 204 (2019) 13–22.
- [19] A. D’Alessio, A. D’Anna, P. Minutolo, L. A. Sgro, Nanoparticles of organic carbon (NOC) formed in flames and their effects in urban atmospheres, in: H. Bockhorn, A. D’Anna, A. Sarofim, H. Wang (Eds.), *Combustion Generated Fine Carbonaceous Particles*, KIT Scientific Publishing (ISBN: 978-3-86644-441-6), 2009, pp. 205–230.

- [20] J. Yon, A. Bescond, F.-X. Ouf, A simple semi-empirical model for effective density measurements of fractal aggregates, *J. Aerosol Sci.* 87 (2015) 28 – 37.
- [21] F.-X. Ouf, S. Bourrous, S. Fauvel, A. Kort, L. Lintis, J. Nuvoli, J. Yon, True density of combustion emitted particles: A comparison of results highlighting the influence of the organic contents, *J. Aerosol Sci.* 134 (2019) 1–13.
- [22] F. Liu, J. Yon, A. Fuentes, P. Lobo, G. J. Smallwood, J. C. Corbin, Review of recent literature on the light absorption properties of black carbon: Refractive index, mass absorption cross section, and absorption function, *Aerosol Sci. Tech.* 54 (2020) 33–51.
- [23] A. D’Anna, A. Rolando, C. Allouis, P. Minutolo, A. D’Alessio, Nano-organic carbon and soot particle measurements in a laminar ethylene diffusion flame, *Proc. Combust. Inst.* 30 (2005) 1449–1456.
- [24] T. W. Kirchstetter, T. Novakov, P. V. Hobbs, Evidence that the spectral dependence of light absorption by aerosols is affected by organic carbon, *Journal of Geophysical Research: Atmospheres* 109 (2004).
- [25] G. Lefevre, J. Yon, F. Liu, A. Coppalle, Spectrally resolved light extinction enhancement of coated soot particles, *Atmos. Environ.* 186 (2018) 89–101.
- [26] M. Schnaiter, M. Gimmler, I. Llamas, C. Linke, C. Jäger, H. Mutschke, Strong spectral dependence of light absorption by organic carbon particles formed by propane combustion, *Atmos. Chem. Phys* 6 (2006) 2981–2990.
- [27] S. Török, V. B. Malmborg, J. Simonsson, A. Eriksson, J. Martinsson, M. Mannazhi, J. Pagels, P.-E. Bengtsson, Investigation of the absorption ångström exponent and its relation to physicochemical properties for mini-cast soot, *Aerosol Science and Technology* 52 (2018) 757–767.
- [28] F. Migliorini, S. De Iuliis, R. Dondè, M. Commodo, P. Minutolo, A. D’Anna, Nanosecond laser irradiation of soot particles: Insights on structure and optical properties, *Exp. Therm. Fluid Sci.* 114 (2020) 110064.

- [29] J. Simonsson, N.-E. Olofsson, S. Török, P.-E. Bengtsson, H. Bladh, Wavelength dependence of extinction in sooting flat premixed flames in the visible and near-infrared regimes, *Appl. Phys. B* 119 (2015) 657–667.
- [30] E. Therssen, Y. Bouvier, C. Schoemaeker-Moreau, X. Mercier, P. Desgroux, M. Ziskind, C. Focsa, Determination of the ratio of soot refractive index function $e(m)$ at the two wavelengths 532 and 1064 nm by laser induced incandescence, *Appl. Phys. B* 89 (2007) 417–427.
- [31] G. Cléon, T. Amodeo, A. Faccineto, P. Desgroux, Laser induced incandescence determination of the ratio of the soot absorption functions at 532 nm and 1064 nm in the nucleation zone of a low pressure premixed sooting flame., *Appl. Phys. B* 104 (2011).
- [32] X. López-Yglesias, P. E. Schrader, H. A. Michelsen, Soot maturity and absorption cross sections, *J. Aerosol Sci.* 75 (2014) 43–64.
- [33] M. Leschowski, K. A. Thomson, D. R. Snelling, C. Schulz, G. J. Smallwood, Combination of LII and extinction measurements for determination of soot volume fraction and estimation of soot maturity in non-premixed laminar flames, *Appl. Phys. B* 119 (2015) 685–696.
- [34] C. Betrancourt, X. Mercier, F. Liu, P. Desgroux, Quantitative measurement of volume fraction profiles of soot of different maturities in premixed flames by extinction-calibrated laser-induced incandescence, *Appl. Phys. B* 125 (2019) 16.
- [35] T. Ishiguro, Y. Takatori, K. Akihama, Microstructure of diesel soot particles probed by electron microscopy: first observation of inner core and outer shell, *Combust. Flame* 108 (1997) 231 – 234.
- [36] A. O. Abdalla, Y. Ying, B. Jiang, X. He, D. Liu, Comparative study on characteristics of soot from n-decane and rp-3 kerosene normal/inverse diffusion flames, *J. Energy Inst.* 93 (2020) 62–75.
- [37] M. R. Kholghy, A. Veshkini, M. J. Thomson, The core–shell internal nanostructure of soot—a criterion to model soot maturity, *Carbon* 100 (2016) 508–536.
- [38] K. C. Le, T. Pino, J. Henriksson, S. Török, P.-E. Bengtsson, et al., Raman spectroscopy of mini-cast soot with various fractions of organic

- compounds: Structural characterization during heating treatment from 25°C to 1000°C, *Combustion and Flame* 209 (2019) 291–302.
- [39] M. Knauer, M. Carrara, D. Rothe, R. Niessner, N. P. Ivleva, Changes in structure and reactivity of soot during oxidation and gasification by oxygen, studied by micro-raman spectroscopy and temperature programmed oxidation, *Aerosol Sci. Tech.* 43 (2009) 1–8.
- [40] A. Bescond, J. Yon, F.-X. Ouf, C. Rozé, A. Coppalle, P. Parent, D. Ferry, C. Laffon, Soot optical properties determined by analyzing extinction spectra in the visible near-UV: Toward an optical speciation according to constituents and structure, *J. Aerosol Sci.* 101 (2016) 118–132.
- [41] M. Alfé, B. Apicella, R. Barbella, J.-N. Rouzaud, A. Tregrossi, A. Ciajolo, Structure–property relationship in nanostructures of young and mature soot in premixed flames, *Proc. of Comb. Inst.* 32 (2009) 697–704.
- [42] Z. Li, L. Qiu, X. Cheng, Y. Li, H. Wu, The evolution of soot morphology and nanostructure in laminar diffusion flame of surrogate fuels for diesel, *Fuel* 211 (2018) 517–528.
- [43] F.-X. Ouf, P. Parent, C. Laffon, I. Marhaba, D. Ferry, B. Marcillaud, E. Antonsson, S. Benkoula, X.-J. Liu, C. Nicolas, et al., First in-flight synchrotron x-ray absorption and photoemission study of carbon soot nanoparticles, *Scientific reports* 6 (2016) 36495.
- [44] S. Lim, T. Ahn, S. Lee, S. Park, Optical measurement of volume fraction and organic mass fraction of ultra-fine soot particles emitted from inverse diffusion flames, *Fuel* 210 (2017) 455–462.
- [45] M. L. Botero, Y. Sheng, J. Akroyd, J. Martin, J. A. Dreyer, W. Yang, M. Kraft, Internal structure of soot particles in a diffusion flame, *Carbon* 141 (2019) 635–642.
- [46] J. Davis, E. Molnar, I. Novosselov, Nanostructure transition of young soot aggregates to mature soot aggregates in diluted diffusion flames, *Carbon* 159 (2020) 255–265.

- [47] D. Cortés, J. Morán, F. Liu, F. Escudero, J. L. Consalvi, A. Fuentes, Effect of Fuels and Oxygen Indices on the Morphology of Soot Generated in Laminar Coflow Diffusion Flames, *Energy Fuels* 32 (2018).
- [48] B. Gigone, A. E. Karataş, Ö. L. Gülder, Soot aggregate morphology in coflow laminar ethylene diffusion flames at elevated pressures, *Proc. Combust. Inst.* 37 (2019) 841–848.
- [49] M. Lapuerta, J. Rodríguez-Fernández, J. Sánchez-Valdepeñas, Soot reactivity analysis and implications on diesel filter regeneration, *Prog. Energy Combust. Sci.* 78 (2020) 100833.
- [50] H. Michelsen, C. Schulz, G. Smallwood, S. Will, Laser-induced incandescence: Particulate diagnostics for combustion, atmospheric, and industrial applications, *Prog. Energy Combust. Sci.* 51 (2015) 2–48.
- [51] R. L. Vander Wal, T. Ticich, A. Stephens, Optical and microscopy investigations of soot structure alterations by laser-induced incandescence, *Applied Physics B* 67 (1998) 115–123.
- [52] Ü. Ö. Köylü, G. M. Faeth, Spectral extinction coefficients of soot aggregates from turbulent diffusion flames, *J. Heat Trans.* 118 (1996) 415–421.
- [53] G. Legros, Q. Wang, J. Bonnetty, M. Kashif, C. Morin, J.-l. Consalvi, F. Liu, Simultaneous soot temperature and volume fraction measurements in axis-symmetric flames by a two-dimensional modulated absorption/emission technique, *Combustion and Flame* 162 (2015) 2705–2719.
- [54] D. Snelling, K. Thomson, G. Smallwood, Ömer Gülder, Two-dimensional imaging of soot volume fraction in laminar diffusion flames, *Appl. Opt.* 38 (1999) 2478–2485.
- [55] F. Escudero, A. Fuentes, R. Demarco, J.-L. Consalvi, F. Liu, J. Elicer-Cortés, C. Fernandez, Effects of oxygen index on soot production and temperature in an ethylene inverse diffusion flame, *Exp. Therm. Fluid Sci.* 73 (2016) 101–108.
- [56] F. Escudero, A. Fuentes, J.-L. Consalvi, F. Liu, R. Demarco, Unified behavior of soot production and radiative heat transfer in ethylene,

- propane and butane axisymmetric laminar diffusion flames at different oxygen indices, *Fuel* 183 (2016) 668 – 679.
- [57] K. J. Daun, K. A. Thomson, F. Liu, G. J. Smallwood, Deconvolution of axisymmetric flame properties using tikhonov regularization, *Appl. Opt.* 45 (2006) 4638–4646.
- [58] E. O. Åkesson, K. J. Daun, Parameter selection methods for axisymmetric flame tomography through tikhonov regularization, *Appl. Opt.* 47 (2008) 407–416.
- [59] P. C. Hansen, D. P. O’Leary, The use of the L-Curve in the regularization of discrete Ill-Posed problems, *SIAM J. Sci. Comput.* 14 (1993) 1487–1503.
- [60] N. Eaves, Q. Zhang, F. Liu, H. Guo, S. Dworkin, M. Thomson, CoFlame: A refined and validated numerical algorithm for modeling sooting laminar coflow diffusion flames, *Comput. Phys. Commun.* 207 (2016) 464–477.
- [61] E. Nordström, N.-E. Olofsson, J. Simonsson, J. Johnsson, H. Bladh, P.-E. Bengtsson, Local gas heating in sooting flames by heat transfer from laser-heated particles investigated using rotational cars and lii, *Proc. Combust. Inst.* 35 (2015) 3707–3713.
- [62] R. Rabello de Castro, L. F. Figueira da Silva, Experimental study of soot volume fraction and temperature of laminar non-premixed ethylene-air flames, in: 24th ABCM International Congress of Mechanical Engineering, 2019, pp. 1–8.
- [63] F. Migliorini, K. A. Thomson, G. J. Smallwood, Investigation of optical properties of aging soot, *Appl. Phys. B* 104 (2011) 273–283.
- [64] K. A. Thomson, M. R. Johnson, D. R. Snelling, G. J. Smallwood, Diffuse-light two-dimensional line-of-sight attenuation for soot concentration measurements, *Appl. Opt.* 47 (2008) 694–703.
- [65] C. Schulz, B. F. Kock, M. Hofmann, H. Michelsen, S. Will, B. Bougie, R. Suntz, G. Smallwood, Laser-induced incandescence: recent trends and current questions, *Appl. Phys. B* 83 (2006) 333.

- [66] Q. Zhang, H. Guo, F. Liu, G. J. Smallwood, M. J. Thomson, Modeling of soot aggregate formation and size distribution in a laminar ethylene/air coflow diffusion flame with detailed PAH chemistry and an advanced sectional aerosol dynamics model, *Proc. Combust. Inst.* 32 (2009) 761–768.
- [67] N. A. Eaves, A. Veshkini, C. Riese, Q. Zhang, S. B. Dworkin, M. J. Thomson, A numerical study of high pressure, laminar, sooting, ethane-air coflow diffusion flames, *Combust. Flame* 159 (2012) 3179–3190.
- [68] M. Saffaripour, M. Kholghy, S. B. Dworkin, M. J. Thomson, A numerical and experimental study of soot formation in a laminar coflow diffusion flame of a Jet A-1 surrogate, *Proc. Combust. Inst.* 34 (2013) 1057–1065.
- [69] N. A. Slavinskaya, P. Frank, A modelling study of aromatic soot precursors formation in laminar methane and ethene flames, *Combust. Flame* 156 (2009) 1705–1722.
- [70] S. B. Dworkin, Q. Zhang, M. J. Thomson, N. A. Slavinskaya, U. Riedel, Application of an enhanced PAH growth model to soot formation in a laminar coflow ethylene/air diffusion flame, *Combust. Flame* 158 (2011) 1682–1695.
- [71] J. Appel, H. Bockhorn, M. Frenklach, Kinetic modeling of soot formation with detailed chemistry and physics: Laminar premixed flames of C2 hydrocarbons, *Combust. Flame* 121 (2000) 122–136.
- [72] F. Liu, H. Guo, G. Smallwood, Effects of radiation model on the modeling of a laminar coflow methane/air diffusion flame, *Combust. Flame* 138 (2004) 136–154.
- [73] F. Liu, G. J. Smallwood, O. L. Gülder, Band Lumping Strategy for Radiation Heat Transfer Calculations Using a Narrowband Model, *J. Thermophys. Heat Trans.* 14 (2000) 278–281.
- [74] Ü. Ö. Köylü, G. Faeth, Optical properties of overfire soot in buoyant turbulent diffusion flames at long residence times, *ASME J Heat Transfer* 116 (1994) 152–159.

- [75] F. Liu, K. A. Thomson, G. J. Smallwood, Effects of soot absorption and scattering on LII intensities in laminar coflow diffusion flames, *Journal of Quantitative Spectroscopy and Radiative Transfer* 109 (2008) 337–348.
- [76] D. D. Hickstein, S. T. Gibson, R. Yurchak, D. D. Das, M. Ryazanov, A direct comparison of high-speed methods for the numerical abel transform, *Rev. Sci. Instrum.* 90 (2019) 065115.
- [77] J. A. Dreyer, R. I. Slavchov, E. J. Rees, J. Akroyd, M. Salamanca, S. Mosbach, M. Kraft, Improved methodology for performing the inverse abel transform of flame images for color ratio pyrometry, *Appl. Opt.* 58 (2019) 2662–2670.